The Astrophysical Journal, 711:990–996, 2010 March 10 doi:10.1088/0004-637X/711/2/990

COUPLED ALFVÉN AND KINK OSCILLATIONS IN CORONAL LOOPS

D. J. Pascoe, A. N. Wright, and I. De Moortel
School of Mathematics and Statistics, University of St Andrews, St Andrews, KY16 9SS, UK; dpascoe@mcs.st-andrews.ac.uk
Received 2009 October 12; accepted 2010 January 27; published 2010 February 19

ABSTRACT

Observations have revealed ubiquitous transverse velocity perturbation waves propagating in the solar corona. However, there is ongoing discussion regarding their interpretation as kink or Alfvén waves. To investigate the nature of transverse waves propagating in the solar corona and their potential for use as a coronal diagnostic in MHD seismology, we perform three-dimensional numerical simulations of footpoint-driven transverse waves propagating in a low β plasma. We consider the cases of both a uniform medium and one with loop-like density structure and perform a parametric study for our structuring parameters. When density structuring is present, resonant absorption in inhomogeneous layers leads to the coupling of the kink mode to the Alfvén mode. The decay of the propagating kink wave as energy is transferred to the local Alfvén mode is in good agreement with a modified interpretation of the analysis of Ruderman & Roberts for standing kink modes. Numerical simulations support the most general interpretation of the observed loop oscillations as a coupling of the kink and Alfvén modes. This coupling may account for the observed predominance of outward wave power in longer coronal loops since the observed damping length is comparable to our estimate based on an assumption of resonant absorption as the damping mechanism.

Key words: magnetohydrodynamics (MHD) – Sun: atmosphere – Sun: corona – Sun: magnetic topology – Sun: oscillations – waves

1. INTRODUCTION

Recent observations by Tomczyk et al. (2007) show that wave activity is ubiquitous in the solar corona. Their observations with the ground-based coronagraph *CoMP* show transverse oscillations propagating outwards everywhere. The waves were initially reported to have phase speeds of about 1–4 Mm s^{-1}, but improved analysis by Tomczyk & McIntosh (2009) gives about 0.6 Mm s^{-1}.

Since the observed phase speed is approximately constant in time, Tomczyk & McIntosh (2009) suggest that the waveguide and driving mechanism are also stable over the same timescale. However, there is a disparity between outward-propagating and inward-propagating wave power, the outward power being much larger. The fact that this occurs along closed loops suggests significant attenuation in situ.

Other properties of the waves are: a broad power spectrum with a peak period of about 5 minutes; propagation along field lines; a correlation length greater than the correlation width, i.e., they are extended along magnetic field.

In Tomczyk et al. (2007), the propagating waves were interpreted as Alfvén waves but this was disputed by Van Doorsselaere et al. (2008a, 2008b) who interpret them as kink waves. These different interpretations have consequences for the inferred coronal magnetic field strength and the energy budget calculations for the coronal heating problem.

Ruderman & Roberts (2002) show how resonant absorption can damp coronal loop oscillations. Their work was motivated by the global standing kink modes as seen by *TRACE*, and is similar to the Edwin & Roberts (1983) configuration except for the inclusion of an inhomogeneous layer of thickness l. Resonant absorption takes place in this inhomogeneous layer, transferring energy from the global kink mode to the Alfvén mode. The decay time depends on the internal and external densities, the thickness of the layer, and the period. By applying this to an observed global kink oscillation, they calculated the layer thickness l (normalized to the tube radius a) as being $l/a \approx 0.23$ assuming resonant absorption was responsible for the rapid decay of the oscillation. Goossens et al. (2002a) performed the same analysis for 11 loops and found l/a in the range 0.15–0.5 by assuming a density contrast $\rho_0/\rho_e = 10$. Arregui et al. (2007a) considered the same data set without assuming this density contrast.

Terradas et al. (2008) considered excitation and damping of transverse standing oscillations in a multi-stranded model of 10 strands with individual densities and radii. They found that the two dominant frequencies found are the global mode and local Alfvén frequency. They found that mode conversion was not compromised by the complicated structure and in fact in this type of configuration resonant absorption can occur at locations within the structure as well as at the external edge since this region also happens to satisfy the condition that the global mode frequency matches the local Alfvén frequency. This result is consistent with that of Russell & Wright (2010) who demonstrated the persistence of resonant wave coupling in equilibria with a two-dimensional structure perpendicular to the background magnetic field. Arregui et al. (2007b) also considered the effect of internal density structuring of a coronal loop on its oscillatory properties using a two-slab model. They found that the internal structure did not significantly affect the features of the resonantly damped fast mode oscillations (see also Goossens et al. 2008).

The simulations of a cylindrical flux tube discussed in this paper can be regarded as complementing the simulations and modeling of a Cartesian (slab) flux tube performed by Wright et al. (1999), Allan & Wright (1998, 2000), and Wright & Allan (2008). The context of these studies was the Earth's magnetotail, part of the Earth's magnetosphere which has a rich history of MHD wave coupling studies (see, e.g., the review by Wright & Mann 2006).

Our studies show that the transverse waves we launch from the boundary couple efficiently to Alfvén waves when the medium is non-uniform. This is seen as a decay of the driven wave fields. Once the energy is in the form of Alfvén waves, it is well known that these fields will phase mix (Heyvaerts & Priest

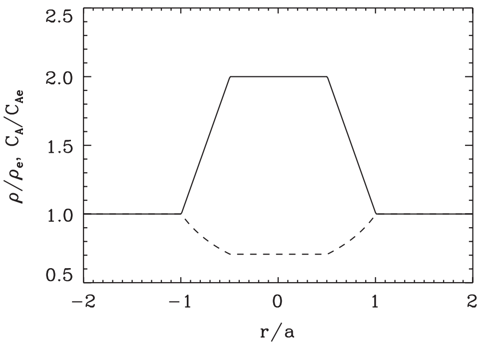

Figure 1. Density profile for the case $\rho_0/\rho_e = 2$ and $l/a = 0.5$ (solid line). The density structure reduces the local Alfvén speed (dashed line).

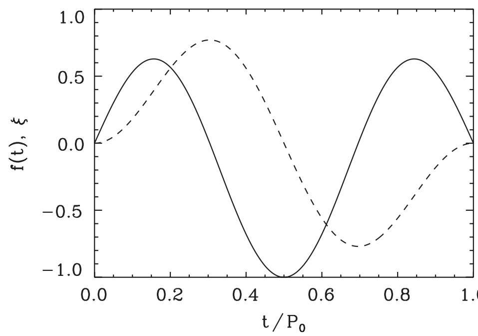

Figure 2. Time dependence of our driver. The dashed line represents the displacement (ξ) of the tube axis. The corresponding velocity dependence ($f(t)$) is given by the solid line.

1983) and lead to the development of small transverse scales. This is true of both standing Alfvén waves (Mann et al. 1995; Poedts et al. 1990) and propagating Alfvén waves (Heyvaerts & Priest 1983; De Moortel et al. 1999, 2000; Hood et al. 2002, 2005). These waves may become Kelvin–Helmholtz unstable (Allan & Wright 1997; Browning & Priest 1984) or develop large currents and lose energy through Joule heating.

The paper is organized as follows. The method of generating an equilibrium state and our driver are described in Section 2. In Section 3, the results of a parametric study are presented. We discuss our results in terms of application to observed coronal wave activity in Section 4, and Section 5 contains our conclusions.

2. MODEL

Considering a global kink standing mode in a zero β cylindrical flux tube with an inhomogeneous layer, Ruderman & Roberts (2002) derived the relationship

$$\frac{\tau}{P} = C\frac{a}{l}\frac{\rho_0 + \rho_e}{\rho_0 - \rho_e}, \tag{1}$$

where τ is the damping time, P is the period of oscillation, a is the loop radius, l is the inhomogeneous layer thickness, and ρ_0 and ρ_e are the internal and external mass densities, respectively. The constant C depends upon the density profile in the inhomogeneous layer. For a sinusoidal density profile in the inhomogeneous layer $C = 2/\pi$, whereas for a linear density profile $C = (2/\pi)^2$ (see, e.g., Hollweg & Yang 1988; Goossens et al. 1992; Roberts 2004, 2008). The key parameters we shall consider are therefore the density contrast ratio ρ_0/ρ_e and the thickness of the inhomogeneous layer l. In the following numerical simulations, we use a linear density profile as its constant gradient is more readily resolved numerically, since it produces uniform phase mixing.

2.1. Equilibrium

In our model, we consider a straight, uniform magnetic field in the z-direction. We use a zero plasma β approximation. Our density profile describes a cylindrical tube aligned with the z-axis and defines three regions: the core region with an internal density ρ_0, the external or environment region with density ρ_e, and the inhomogeneous shell region in between, where the density varies linearly from ρ_0 to ρ_e:

$$\rho = \begin{cases} \rho_0 & \text{if } r \leqslant b < a \\ \rho_0 + (\rho_e - \rho_0)(r - b)/l & \text{if } b < r \leqslant a \\ \rho_e & \text{if } r > a, \end{cases} \tag{2}$$

where $r = \sqrt{x^2 + y^2}$ and $l = a - b$. For $\rho_0 > \rho_e$, the structure is a minimum in the Alfvén speed and so a waveguide for MHD waves (see, e.g., Edwin & Roberts 1983; Roberts et al. 1984). The density and Alfvén speed profiles are shown in Figure 1 for the case $\rho_0/\rho_e = 2$ and $l/a = 0.5$.

2.2. Driver

The driving condition is applied to the lower z boundary to simulate excitation by footpoint motions (e.g., De Groof et al. 2002) and prescribes the x and y components of velocity to have a time dependence $f(t)$:

$$\mathbf{v} = f(t)\mathbf{u}, \ \ \mathbf{u} = (u_x, u_y, 0). \tag{3}$$

The time dependence of our driver is based on a single period displacement of the loop axis and is shown in Figure 2. The dashed line shows the time variation of our displacement $\xi \propto \sin(\omega t)$ combined with an envelope of $\sin(2\omega t)$ to provide the smooth ramp up and down at the beginning and end of the driving phase. The corresponding velocity dependence is calculated as the time derivative $f(t) = \frac{d\xi}{dt}$ shown by the solid line.

The driven velocity time dependence therefore has three stages: an initial positive stage that displaces the loop axis, followed by a larger negative stage that takes the loop axis back through the starting point and then displaces it in the opposite direction. A final positive stage then returns the loop axis to its starting position. Note also that due to the non-harmonic nature of the driver the driving time P_0 is not directly equivalent to the period of oscillation. By considering the three-staged $f(t)$, we may estimate the dominant period of oscillation in a Fourier spectrum as $P \approx \frac{2}{3}P_0$.

The spatial dependence of the driver is based on a two-dimensional dipole. In the core region the velocity is constant $\mathbf{u} = (u_0, 0, 0)$ and only in the x-direction, where $u_0 = 0.002$ is chosen to be small to avoid nonlinear effects. In the surrounding environment we have the two-dimensional dipole form:

$$\mathbf{u} = u_0 a^2 \left(\frac{x^2 - y^2}{(x^2 + y^2)^2}, \frac{2xy}{(x^2 + y^2)^2}, 0 \right). \tag{4}$$

The flow described so far corresponds to two-dimensional incompressible dipole flow around a circular tube that moves with velocity $(u_0, 0, 0)$. In cylindrical coordinates, this would be described as the $m = 1$ mode, in which u_r is continuous and u_ϕ discontinuous at the tube boundary.

To avoid numerical problems with velocity components that are discontinuous, we introduce a velocity transition region that

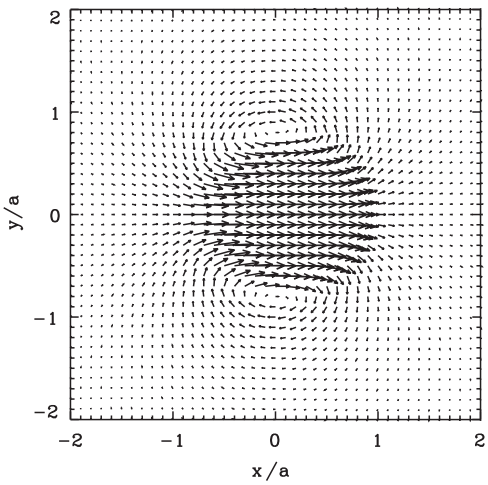

Figure 3. Spatial dependence of our driver. The arrows describe the velocity field at $t = P_0/6$ (for $l/a = 0.5$).

coincides with the shell over which the density changes. Within the shell region, we change smoothly from the solution for the core to that for the environment. Figure 3 shows the velocity field at $t = P_0/6$ for $l/a = 0.5$.

The simulations are performed using the MHD code Lare3D (Arber et al. 2001). The numerical domain is much larger in the z-direction than in x or y, but the resolution is higher in the x- and y-directions as our main priority is resolving the activity in the inhomogeneous layer. Typical values used are $400 \times 400 \times 200$ grid points for a numerical domain $4 \times 4 \times 20$ Mm ($a = 1$ Mm).

The boundary conditions are periodic in the x- and y-directions, although these have little influence. Initially the lower z boundary is driven, but after our driving phase (see Figure 2) the driver is turned off and the z boundaries also become periodic. This allows the pulse to propagate out of the top of our domain and simply cycle through by re-entering at the lower boundary. This is a numerically efficient way of avoiding a large domain in the field-aligned direction (z).

3. RESULTS

In the case of a uniform medium ($\rho_0/\rho_e = 1$), the Alfvén speed is constant everywhere. From $t = 0$ to $t = P_0 = 10$ s (for a normalization based on an external Alfvén speed $C_{Ae} = 1$ Mm s^{-1} and $a = 1$ Mm), the driver is applied at the lower z boundary as described in Section 2.2. The perturbation at the lower boundary propagates upwards uniformly (see Figure 4). After $t = P_0$, the driver stops and the upper and lower boundaries become periodic. The wavetrain continues to propagate in the z domain and at later times demonstrates a very small amount of dispersion due to numerical effects. Figure 4 shows v_x in the $x = 0$ plane at time $t = P_0$ for a uniform medium ($\rho_0/\rho_e = 1$). Also shown is the same wavetrain at the later time $t = 5P_0$, by which time it has propagated through the upper boundary and re-emerged from the lower boundary. The wavetrain does not show signs of any significant attenuation or dispersion.

The driven perturbations in this case are Alfvénic and do not couple to any other mode. This solution is similar to the "Alfvén wings" that are established on the field lines disturbed by the "Io flux tube" in the Jovian magnetosphere (see Neubauer 1980; Wright & Southwood 1987).

Although we do not drive the boundary for many cycles, and hence do not have a quasi-monochromatic source, the driver does have a well-defined nodal structure and is dominated by a timescale of $P \approx \frac{2}{3}P_0$. Indeed, we could think of having a broadband driver with power concentrated at a frequency of $f_d = \frac{3}{2}f_0$, where $f_0 = P_0^{-1}$. The Alfvén wave dispersion relation can then be used to infer the parallel wavelength of the driven wave packet to be $\lambda_d = C_A P \approx 7$, in agreement with the structure visible in Figure 4.

In the case of an inhomogeneous layer ($\rho_0/\rho_e > 1$) the simulation proceeds in the same way. However, as the driver acts over all three density regions, the Alfvén speed now varies for different regions of the driver (see Figure 1). The Alfvén speed $C_A(\mathbf{r})$ varies continuously in the inhomogeneous layer and resonant absorption occurs where the condition $\omega = C_A(\mathbf{r})k_z$ is satisfied, where ω is the (angular) frequency of oscillation and k_z is the local longitudinal wavenumber.

Figure 5 is a similar format to Figure 4. It shows a wavetrain at the early and late stages for the case of a structured medium with density contrast ratio $\rho_0/\rho_e = 2$. At early times, we already see signs of phase mixing occurring in the inhomogeneous shell region $0.5 < |y| < 1.0$. By the later stage, we see that the wavetrain has undergone complete attenuation in the core region $|y| < 0.5$ and only the strongly phase-mixed Alfvén wave in the shell region remains.

This coupling of the wavetrain to a local Alfvén mode causes a decrease in wave energy in the core (and the environment) and hence appears to damp the tube oscillation. Also, since the Alfvén mode is in an inhomogeneous layer, it is subject to phase mixing. The corresponding characteristic spatial scale becomes smaller as a function of time and when it becomes comparable to the simulation grid scale defines a maximum runtime. We therefore ensure we have sufficient resolution of the inhomogeneous layer that our results do not become unresolved and unphysical.

Fast MHD waves are highly dispersive, i.e., $\omega = \omega(\mathbf{k})$. In considering the wavenumber of our wavetrain parallel to the direction of propagation, $k_{||}$, from the thin tube approximation (Edwin & Roberts 1983) we have

$$\omega \approx k_{||}C_{\mathrm{k}}, \tag{5}$$

where $\omega = 2\pi/P$ and the kink speed is $C_{\mathrm{k}} = \sqrt{2/(1+\rho_e/\rho_0)}C_{A0}$ for the case of a uniform magnetic field $B_0 = B_e$. This approximation is considered in Figure 6, which shows v_x at time $t = 4P_0$ for $\rho_0/\rho_e = 2$ and $l/a = 0.5$ (see Figure 5). v_x is plotted as a function of z at $x = 0$ and in the middle of the inhomogeneous layer, i.e., $y = a - l/2$. The dotted lines mark the maximum and minimum of the wavetrain. The thick horizontal line corresponds to a distance $\lambda_{||}/2$, i.e., the distance between the peak and the subsequent trough, calculated as $\lambda_{||} = 2\pi/k_{||}$ using $k_{||}$ from Equation (5). The two agree surprisingly well, suggesting the thin flux tube results can be a useful guide to interpreting our simulation results. (Note the thin flux tube approximation is valid when $k_z a \ll 1$, whereas in Figure 5 $k_z a \sim 1$.)

Mann et al. (1995) calculated the time dependence of the phase-mixing length L_{ph} as

$$L_{\mathrm{ph}} = \frac{2\pi}{\omega_A' t}, \tag{6}$$

where $\omega_A' \approx k_{||}v_A'$ and $v_A' = dv_A/dr \approx (C_{Ae} - C_{A0})/l$.

Figure 7 shows v_x as a function of y at time $t = 4P_0$ for $\rho_0/\rho_e = 2$ and $l/a = 0.5$. The dashed lines correspond to L_{ph}

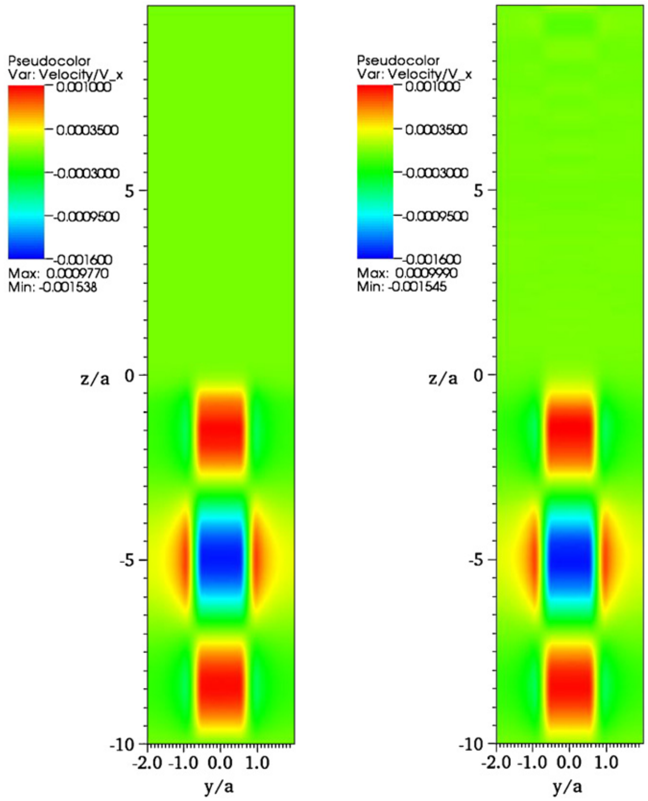

Figure 4. v_x at $x = 0$ and at time $t = P_0$ (left) and $t = 5P_0$ (right) for $\rho_0/\rho_e = 1$ and $l/a = 0.5$.

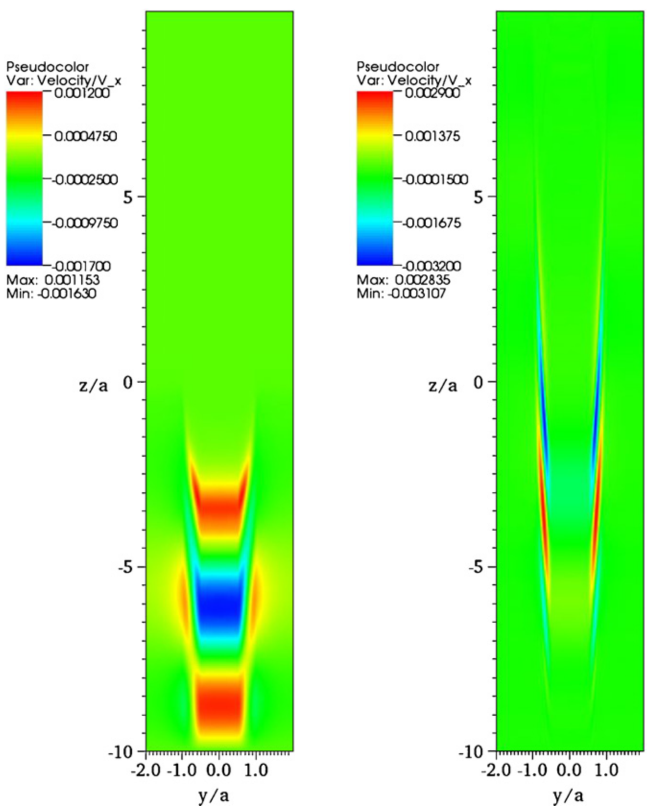

Figure 5. v_x at $x = 0$ and at time $t = P_0$ (left) and $t = 4P_0$ (right) for $\rho_0/\rho_e = 2$ and $l/a = 0.5$.

calculated from Equation (6) and agree well with the transverse wavelength of the phase-mixed Alfvén wave in our simulations.

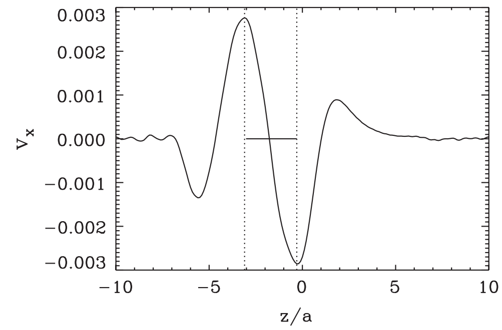

Figure 6. v_x at time $t = 4P_0$ for $\rho_0/\rho_e = 2$ and $l/a = 0.5$ (see Figure 5). v_x is plotted as a function of z at $x = 0$ and for $y = a - l/2$. The dotted lines mark the maximum and minimum of the wavetrain. The thick horizontal line corresponds to $\lambda_{||}/2$ calculated using Equation (5).

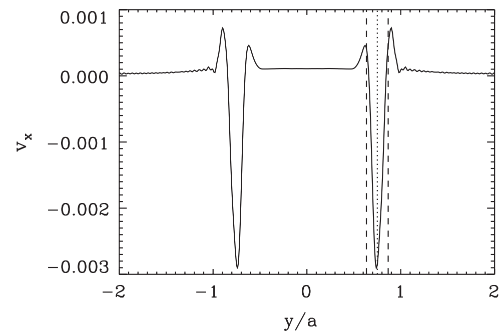

Figure 7. v_x as a function of y at time $t = 4P_0$ for $\rho_0/\rho_e = 2$ and $l/a = 0.5$. The dashed lines correspond to the phase-mixing length L_{ph} calculated from Equation (6).

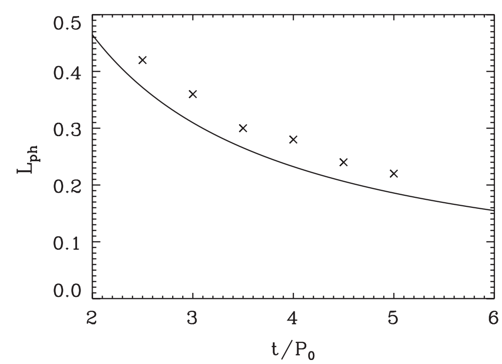

Figure 8. L_{ph} as a function of time for $\rho_0/\rho_e = 2$ and $l/a = 0.5$. The solid line is the analytic expression given by Equation (6).

Figure 8 shows L_{ph} as a function of time for $\rho_0/\rho_e = 2$ and $l/a = 0.5$. The decrease of the phase-mixing length with time is expected since phase mixing generates increasingly large gradients. The dependence is in good agreement with the analytic approximation (solid line) given by Equation (6).

3.1. Decay Rates

In order to quantify the behavior in our model, we calculate the wave energy density as (see also Terradas et al. 2006, 2008)

$$E = \frac{1}{2}\left(\rho\left(v_x^2 + v_y^2 + v_z^2\right) + \frac{1}{\mu}\left(b_x^2 + b_y^2 + b_z^2\right)\right), \qquad (7)$$

where $\mathbf{b}(t) = \mathbf{B}(t) - \mathbf{B}(t = 0)$.

Figure 9 shows the spatially integrated wave energy (normalized) as a function of time for a uniform medium and $\rho_0/\rho_e = 2$. The solid line represents the total wave energy. The integrated

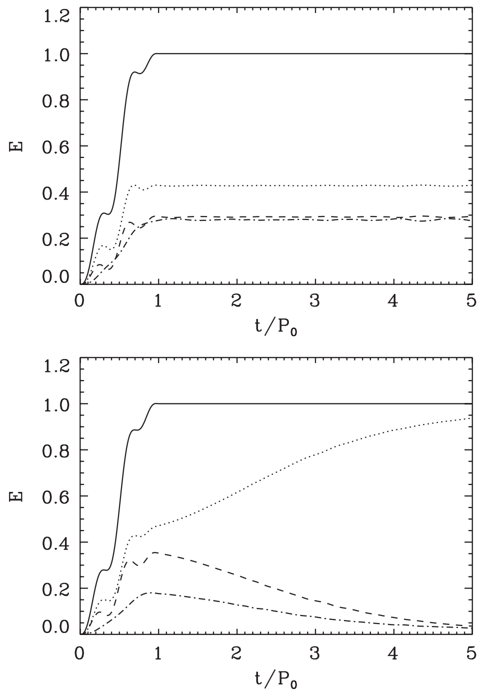

Figure 9. Integrated wave energy (normalized) as a function of time for a uniform medium (top) and $\rho_0/\rho_e = 2$ (bottom). The solid line represents the total integrated wave energy. The integrated wave energy in the core, shell, and environment regions are represented by the dashed, dotted, and dash-dotted lines, respectively.

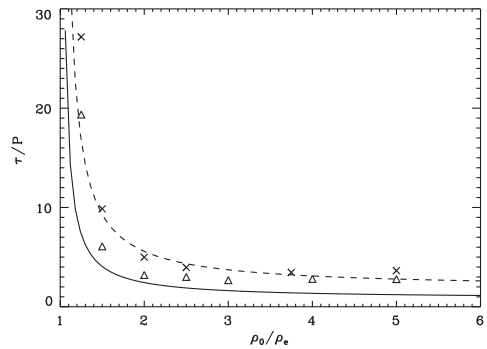

Figure 10. Ratio of damping time (τ) to period of oscillation (P) for the propagating wavetrain (crosses) as a function of density contrast ratio (ρ_0/ρ_e) for $l/a = 0.5$. The solid line represents the analytical relationship derived for standing modes (see Ruderman & Roberts 2002). The dashed line represents a best fit (see Equation (1)). The triangles are for numerical simulations of standing modes having the same parameters as the propagating wavetrains.

wave energy in the core, shell, and environment regions are represented by the dashed, dotted, and dash-dotted lines, respectively. In the uniform case, the wavetrain propagates in the z-direction without modification (see Figure 4) and so is constant in all three regions after the driving phase, i.e., for times $t > P_0$. The two local maxima seen during the driving phase correspond to the time dependence described in Figure 2.

In the non-uniform case, the effect of resonant absorption is readily seen. Mode coupling in the inhomogeneous shell causes the wave energy to become localized there with a corresponding decrease in energy in the core and environment regions. The damping of the wave energy in the core may be quantified by fitting the profile for $t > P_0$ to an exponential decay with decay time τ_E. Note that the decay time of the wave fields will be $\tau = 2\tau_E$ since $E \propto u^2$. Although the energy associated with the kink-like mode clearly decays, it is important to note that we have a decaying propagating wave packet, not a decaying standing mode (upon which the existing literature focuses). However, Hood et al. (2005) show that normal mode calculations can be a surprisingly good indicator of wave packet behavior, when the spatial and temporal scales are similar. With this in mind we compare our wave packet decay rates with the Ruderman & Roberts (2002) formula in Equation (1) with $C = (2/\pi)^2$ (see Figure 10). Given that our simulations are not of a thin flux tube with a thin inhomogeneous layer, or a standing structure, the agreement is surprisingly good. Slightly better agreement is found with additional initial value simulations we performed where the equilibrium was the same, but a standing mode of $\lambda_z = \pi/(PC_{\mathrm{k}})$ was used (see the triangles in Figure 10). It would appear that the vast literature on standing modes could provide a useful guide to wave packets having similar scales.

In order to make further comparison with the analysis of Ruderman & Roberts (2002), we performed a parametric study to investigate the behavior as a function of density contrast ratio and inhomogeneous layer thickness, considering in particular the damping time τ of the core oscillations.

Figure 10 shows the damping per period (τ/P) as a function of density contrast ratio (for $l/a = 0.5$). Note the damping time τ corresponds to the rate of mode conversion rather than, say, viscous damping. The solid line represents the analytical relationship derived for standing modes by Ruderman & Roberts (2002). The dashed line represents a best fit of the asymptotic expression, i.e., Equation (1) with $C = 0.9$. The damping per period depends strongly on the density contrast ratio up to $\rho_0/\rho_e \approx 2$, after which it quickly saturates. The triangles are for numerical simulations of standing modes having the same parameters as the propagating wavetrains, i.e., same value of longitudinal wavenumber k_z and same spatial dependence of the driver $\mathbf{u}$ with $\mathbf{v} = \mathbf{u}\sin(k_z z)$. The standing mode simulations were run as an initial value problem (with $\mathbf{b} = 0$), and the damping rate and period estimated from the time development of the fields. Comparing the results for propagating wavetrains with the numerical and analytical results for standing modes, it can be seen that the normal mode analysis is a useful guide to the behavior of the propagating wave packets. The quantitative difference between the analytical relationship and the numerical standing modes is due to the non-applicability of the analytical approximations, namely a thin tube with a thin inhomogeneous layer. Our results are comparable with Van Doorsselaere et al. (2004) who considered standing modes with a complex frequency in the regime of thick inhomogeneous layers.

Figure 11 shows the damping per period as a function of the inhomogeneous layer thickness (for $\rho_0/\rho_e = 2$). As $l \to 0$, we recover the solution of Edwin & Roberts (1983) for a harmonic kink mode in a magnetic cylinder with $\tau/P \to \infty$. The dashed line represents the best fit of Equation (1) with $C = 0.9$. Note that for our simulations we find $C = 0.9$ for all values of ρ and l considered. Choosing this value of C, the Ruderman & Roberts (2002) result in Equation (1) can be regarded as providing an empirical fit to our simulation results. That the value of C differs from that in the Ruderman & Roberts (2002) calculation can be attributed to the fact that our model is not accurately described as a thin flux tube with a thin boundary layer.

4. DISCUSSION

In Section 3, we showed how our non-monochromatic driver on the lower boundary produced an upwardly propagating

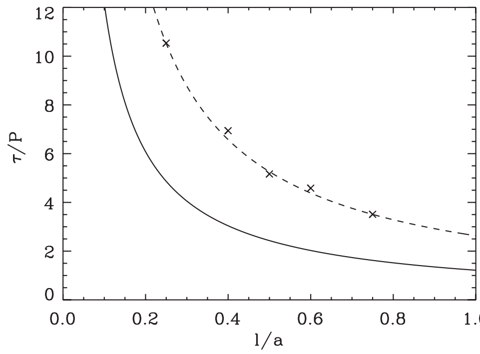

Figure 11. Damping per period as a function of inhomogeneous layer thickness l for $\rho_0/\rho_e = 2$. The loop width a is 1 Mm. Solid and dashed lines are as in Figure 10.

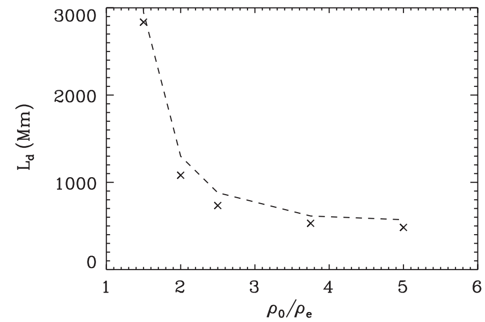

Figure 12. Damping length for a transverse wave packet propagating in the solar corona as a function of density contrast ratio. The dashed line shows an analytic estimate.

wavetrain. In the case of a non-uniform medium, the wavetrain was subject to mode coupling through resonant absorption. Here we will discuss these results in the context of the observations of Tomczyk et al. (2007) and the interpretation of Van Doorsselaere et al. (2008a, 2008b) as kink waves. In this case, our driver corresponds to some general photospheric motion and our wavetrain corresponds to the Doppler shift in coronal emission observed by Tomczyk et al. (2007).

Damping of transverse waves propagating in the solar corona is reported by Tomczyk & McIntosh (2009). We have demonstrated that such waves propagating in a medium with transverse structure in density (and hence Alfvén speed) will undergo damping due to resonant absorption. By considering Equation (1) we can see a finite damping time will occur in all but two specific cases: the homogeneous case ($\rho_0 - \rho_e = 0$) and the case of a perfectly discontinuous density profile ($l = 0$). In the homogeneous case, the Alfvén speed profile is uniform and the transverse velocity wavetrain corresponds to an undamped propagating Alfvén wave with a two-dimensional dipolar flow pattern ($m = 1$) outside the tube (e.g., Neubauer 1980; Wright & Southwood 1987). In the limit of $l \to 0$, we recover the analytical model of Edwin & Roberts (1983) and the mode perturbing the loop axis is described as an undamped kink mode. There is also an Alfvén wave corresponding to the uncoupled $m = 0$ which is a torsional oscillation of the flux tube (Spruit & van Ballegooijen 1982).

In the most general case of a continuously non-uniform corona, we expect the behavior demonstrated by our numerical simulations: that of a quasi-mode composed of the kink mode coupled to the Alfvén mode. Due to resonant absorption and the introduction of a characteristic (damping) time (τ) the time-dependent nature of the mode must be considered. In the limit $t > \tau$ resonant absorption leads to the wave energy being concentrated in the Alfvén mode, whereas for $t < \tau$ the behavior is described by the kink mode of Edwin & Roberts (1983). The coupled nature of MHD waves in a non-uniform plasma is also discussed by Goossens et al. (2002b, 2009).

According to this interpretation, the transverse waves observed by Tomczyk et al. (2007) are in the regime $t \approx \tau$ and so are an intrinsically coupled mode. This will be true even for a very weak density contrast. The properties of the observed Doppler shifts will predominantly *resemble* a kink mode. The coupled Alfvén mode component is generally unresolved by modern solar instruments, and so will contribute to the Doppler shifts incoherently. However, its presence is necessary to explain the rapid damping. Jess et al. (2009) report the possible observation of a torsional Alfvén mode in the lower solar atmosphere.

Figure 12 shows the damping length as a function of the density contrast ratio, based on our numerical results and the observed period $P \approx 300$ s (Tomczyk & McIntosh 2009). The dashed line shows the analytic estimate $L_d = V_g\tau$, where V_g is the group speed of the wavetrain. We see that resonant absorption becomes effective for modest density contrasts of 2–3 and tends quickly to an asymptotic value. Here we have assumed $l/a = 0.5$, typical for our numerical simulations, but only expect τ to vary linearly with a/l. Based on this estimate, if resonant absorption is responsible for the damping then we expect $L_d \approx 750$ Mm as a lower limit. If we consider closed loop structures, this would correspond to a footpoint separation of $2L_d/\pi \approx 500$ Mm. Tomczyk & McIntosh (2009) show in their Figure 7(c) that the outward-directed wave velocity power dominates the inward-directed power for loop structures with a footpoint separation greater than 300 Mm. For loops smaller than this, the outward and inward wave powers are similar in magnitude. This simple estimate of damping length scales is therefore consistent with observations: loops that are small (compared to the damping length) will have a stronger inward propagating component than loops that are large (compared to the damping length), or flux tubes that are open.

5. CONCLUSIONS

We have performed three-dimensional numerical simulations of footpoint-driven transverse waves propagating in a low β plasma. This is motivated by the observations of ubiquitous transverse velocity waves propagating in the solar corona. We have both considered the case of a uniform medium, and performed a parametric study for a field-aligned, loop-like density structure with varying density contrast and inhomogeneity width.

We apply a small amplitude perturbation as our driver corresponding to a transverse displacement of the "loop" axis. When density structuring is present, resonant absorption in the inhomogeneous regions leads to the coupling of the kink mode to the Alfvén mode. The decay of the propagating kink wave as energy is transferred to the local Alfvén mode is in good agreement with a modified interpretation of the analysis of standing kink modes by Ruderman & Roberts (2002).

As mode coupling is present unless the medium is uniform or discontinuous, our work supports the most general interpretation of the observed waves as a coupling of the kink and Alfvén modes. We demonstrated that this coupling can account for the predominance of outward wave power in longer coronal loops as observed by Tomczyk & McIntosh (2009). The damping rate due to resonant absorption depends on the density contrast ratio and the gradient of the density. The observed propagating waves therefore have potential as a coronal diagnostic in MHD coronal seismology, assuming these observations can be repeated for a number of magnetic field configurations and viewing angles allowing our interpretation to be confidently applied. We have also assumed that the background loop structure remains stable over the course of several wave periods.

Although our simulations are for propagating wave packets, we find the results of the existing literature on standing modes can provide a useful guide to our results if the spatial and temporal scales of the pulses and standing modes are matched.

Our assumption of a zero plasma β makes our model more applicable to the solar corona than the lower atmosphere. In future work we will consider the case of a finite plasma β. This will allow us to calculate a temperature profile and use forward modeling (De Moortel & Bradshaw 2008) to predict the observational signature of transverse wavetrains propagating in the solar corona and so allow a direct comparison with observations such as those analyzed by Tomczyk et al. (2007). We will also consider the effects of the Kelvin–Helmholtz instability for large amplitude perturbations.

D.J.P. acknowledges financial support from STFC. I.D.M. acknowledges support of a Royal Society University Research Fellowship. The computational work for this paper was carried out on the joint STFC and SFC (SRIF) funded cluster at the University of St. Andrews (Scotland, UK).

REFERENCES

Allan, W., & Wright, A. N. 1997, J. Geophys. Res., 102, 19927
Allan, W., & Wright, A. N. 1998, J. Geophys. Res., 103, 2359
Allan, W., & Wright, A. N. 2000, J. Geophys. Res., 105, 317
Arber, T. D., Longbottom, A. W., Gerrard, C. L., & Milne, A. M. 2001, J. Comput. Phys., 171, 151
Arregui, I., Andries, J., Van Doorsselaere, T., Goossens, M., & Poedts, S. 2007a, A&A, 463, 333
Arregui, I., Terradas, J., Oliver, R., & Ballester, J. L. 2007b, A&A, 466, 1145
Browning, P. K., & Priest, E. R. 1984, A&A, 131, 283
De Groof, A., Paes, K., & Goossens, M. 2002, A&A, 386, 681
De Moortel, I., & Bradshaw, S. J. 2008, Sol. Phys., 252, 101
De Moortel, I., Hood, A. W., & Arber, T. D. 2000, A&A, 354, 334
De Moortel, I., Hood, A. W., Ireland, J., & Arber, T. D. 1999, A&A, 346, 641
Edwin, P. M., & Roberts, B. 1983, Sol. Phys., 88, 179
Goossens, M., Andries, J., & Aschwanden, M. J. 2002a, A&A, 394, L39
Goossens, M., Arregui, I., Ballester, J. L., & Wang, T. J. 2008, A&A, 484, 851
Goossens, M., De Groof, A., & Andries, J. 2002b, SOLMAG 2002, Proc. Magnetic Coupling Solar Atmosphere Euroconf., ed. H. Sawaya-Lacoste (ESA SP-505; Noordwijk: ESA), 137
Goossens, M., Hollweg, J. V., & Sakurai, T. 1992, Sol. Phys., 138, 233
Goossens, M., Terradas, J., Andries, J., Arregui, I., & Ballester, J. L. 2009, A&A, 503, 213
Heyvaerts, J., & Priest, E. R. 1983, ApJ, 117, 220
Hollweg, J. V., & Yang, G. 1988, J. Geophys. Res., 93, 5423
Hood, A. W., Brooks, S. J., & Wright, A. N. 2002, Proc. R. Soc. Lond. A, 458, 2307
Hood, A. W., Brooks, S. J., & Wright, A. N. 2005, Proc. R. Soc. Lond. A, 461, 237
Jess, D. B., Mathioudakis, M., Erdélyi, R., Crockett, P. J., Keenan, F. P., & Christian, D. J. 2009, Science, 323, 1582
Mann, I.R., Wright, A. N., & Cally, P. S. 1995, J. Geophys. Res., 100, 19441
Neubauer, F. M. 1980, J. Geophys. Res., 85, 1171
Poedts, S., Goossens, M., & Kerner, W. 1990, Comput. Phys. Commun., 59, 95
Roberts, B. 2004, in Proc. SOHO 13, Waves, Oscillations and Small-Scale Transient Events in the Solar Atmosphere: A Joint View from *SOHO* and *TRACE*, ed. H. Lacoste (ESA SP-547; Noordwijk: ESA), P1
Roberts, B. 2008, in IAU Symp. 247, Waves & Oscillations in the Solar Atmosphere: Heating and Magneto-Seismology, ed. R. Erdélyi & C. A. Mendoza-Briceño (Dordrecht: Kluwer), 3
Roberts, B., Edwin, P. M., & Benz, A. O. 1984, ApJ, 279, 857
Ruderman, M. S., & Roberts, B. 2002, ApJ, 577, 475
Russell, A. J. B., & Wright, A. N. 2010, A&A, in press
Spruit, H. C., & van Ballegooijen, A. A. 1982, A&A, 106, 58
Terradas, J., Arregui, I., Oliver, R., & Ballester, J. L. 2008, ApJ, 679, 1611
Terradas, J., Oliver, R., & Ballester, J. L. 2006, ApJ, 642, 533
Tomczyk, S., & McIntosh, S. W. 2009, ApJ, 697, 1384
Tomczyk, S., McIntosh, S. W., Keil, S. L., Judge, P. G., Schad, T., Seeley, D. H., & Edmondson, J. 2007, Science, 317, 1192
Van Doorsselaere, T., Andries, J., Poedts, S., & Goossens, M. 2004, ApJ, 606, 1223
Van Doorsselaere, T., Brady, C. S., Verwichte, E., & Nakariakov, V. M. 2008a, A&A, 491, L9
Van Doorsselaere, T., Nakariakov, V. M., & Verwichte, E. 2008b, ApJ, 676, L73
Wright, A. N., & Allan, W. 2008, J. Geophys. Res., 113, A02206
Wright, A. N., Allan, W., Elphinstone, R. D., & Cogger, L. L. 1999, J. Geophys. Res., 104, 10159
Wright, A. N., & Mann, I. R. 2006, AGU Monograph Ser., 169, 51
Wright, A. N., & Southwood, D. J. 1987, J. Geophys. Res., 92, 1167